

Ultra-low lattice thermal conductivity induces high-performance thermoelectricity in Janus group-VIA binary monolayers

Shao-Bo Chen^{1,2}, San-Dong Guo³, Bing Lv⁴, Mei Xu^{4,*}, Xiang-Rong Chen^{1,*}, and Hua-Yun Geng⁵

¹ College of Physics, Institute of Atomic and Molecular Physics, Sichuan University, Chengdu 610065, Peoples Republic of China

² College of Electronic and Information Engineering, Anshun University, Anshun 561000, Peoples Republic of China

³ School of Electronic Engineering, Xian University of Posts and Telecommunications, Xian 710121, Peoples Republic of China

⁴ School of Physics and Electronic Science, Guizhou Normal University, Guiyang 550025, Peoples Republic of China and

⁵ National Key Laboratory for Shock Wave and Detonation Physics Research, Institute of Fluid Physics, CAEP, Mianyang 621900, Peoples Republic of China

Email: xumei6401@tom.com; xrchen@scu.edu.cn

In this paper, the electrical transport, thermal transport, and thermoelectric properties of three new Janus STe_2 , SeTe_2 , and Se_2Te monolayers are systematically studied by first-principles calculations, as well as the comparative with available literatures results using different methods. It is found that the Seebeck coefficient and conductivity have opposite dependence on temperature, and we illustrate this phenomenon in detail. The decrease of the thermoelectric power factor (PF) with temperature originates from the decrease in conductivity. To obtain accurate and convergent lattice thermal conductivity, the root mean square (RMS) is calculated to obtain a reasonable cutoff radius for the calculation of third-order forces. Janus STe_2 , SeTe_2 , and Se_2Te monolayers exhibit ultra-low lattice thermal conductivity of 0.2, 0.133, and 4.81×10^{-4} W/mK at 300 K, which result from the strong coupling effect between the acoustic mode and the low-frequency optical branch, low phonon group velocity, small phonon lifetime, and large anharmonicity. Consequently, ultra-high ZT values of 2.11 (2.09), 3.28 (4.24), and 3.40 (6.51) for n-type(p-type) carrier doping of STe_2 , SeTe_2 , and Se_2Te are obtained, indicating that they are promising thermoelectric materials.

KEYWORDS — *lattice thermal conductivity; thermoelectricity; group-VIA binary monolayers*

I. INTRODUCTION

Thermoelectric materials have become a hot research topic because they can directly convert heat energy into electric energy. As a new member of the thermoelectric materials family, two-dimensional (2D) materials have attracted extensive attention because of their unique electrical, thermal, and mechanical properties. In the past decades, the 2D thermoelectric materials, such as SnSe , Bi_2Te_3 , and MoS_2 , have been theoretically predicted and the corresponding samples have been experimentally synthesized^{1–3}. These 2D materials exhibit excellent thermoelectric properties and have great potential when they are used to manufacture high-performance thermoelectric devices. However, due to the high thermal conductivity of 2D materials, the thermoelectric properties of 2D materials are still much lower than those of traditional bulk thermoelectric materials, which limits the thermoelectric applications in 2D materials. Since Li et al.^{4,5} successfully synthesized 2D tellurium (Te), its attractive characteristics including thickness-dependent band gap, environmental stability, piezoelectric effect, thermoelectric effect, high carrier mobility, and light response show great potential in photodetectors, field effect transistors, piezoelectric devices, thermoelectric devices, modulators, and energy harvesting devices⁶. 2D allotrope tellurene composed of the metal-

like element Te mainly includes three phases (α , β , and γ). The stable α -Te has the structure of 1T phase MoS_2 , and the metastable β -Te and γ -Te have the structure of the foursquare structure and 2H phase MoS_2 , respectively. Tellurene is a well-known p-type semiconductor with a band gap of 0.35 eV at room temperature. Subsequently, 2D homogeneous selenene (α -Se, β -Se, γ -Se) with the same structure was successively discovered⁷. The 2D material family is enriched again by the appearance of tellurene and selenene. Among these 2D materials composed of a single element, tellurene and selenene have the lowest lattice thermal conductivity among 2D materials reported so far^{7–9}. It has been theoretically and experimentally demonstrated that compounds composed of both Te and Se elements have excellent thermoelectric and electron transport properties^{10,11}. Inspired by the noncentrosymmetric Janus structure have novel properties and group-VIA elements possess ultra-low lattice thermal conductivity, it is envisaged that the Janus-structured binary compounds composed of group-VIA elements (S, Se, Te) have excellent thermoelectricity as a consequence of ultra-low lattice thermal conductivity, which has potential applications in thermoelectric devices. In this paper, we predict three stable group-VIA binary monolayers with ultra-low lattice thermal conductivity and ultra-high thermoelectric performance.

II. CALCULATION DETAILS

All calculations based on the density functional theory are performed in the VASP code¹². The projector-augmented-wave (PAW) pseudopotential is carried out to represent the interaction between the ions and the electrons¹³. The generalized gradient approximation (GGA) within the Perdew-Burke-Ernzerhof (PBE) formulation is employed for the exchange-correlation potential. The second-order force constants (harmonics) are implemented in the PHONOPY code¹⁴ based on density functional perturbation theory (DFPT) using a $5 \times 5 \times 1$ supercells and $3 \times 3 \times 1$ k-point grid. Then, the phonon dispersion relation can be obtained by diagonalizing the force constant matrix. The ab initio molecular dynamics (AIMD) simulations are performed by using the canonical ensemble with a $5 \times 5 \times 1$ supercell and the simulation time is set to 5 ps with the step of 2 fs. Based on Boltzmann transport theory, TransOpt¹⁵ is used to calculate the electrical transport coefficient of the material with constant electron-phonon coupling approximation in the relaxation time approximation method. The third-order force constants (non-harmonics) are calculated using the finite displacement method^{14,16} with a $4 \times 4 \times 1$ supercell and a $3 \times 3 \times 1$ k-point grid. To get the precise lattice thermal conductivity, we separately test the nearest-neighbor interactions and the Q-grid. The lattice thermal conductivity is obtained by iteratively solving the phonon Boltzmann transport equation using the ShengBTE code¹⁷.

III. RESULT AND DISCUSSION

A. Electrical transport properties

There are six different VIA binary monolayers, depending on the combination of different elements. Only three structures are stable after the stability test. The Janus STe₂, SeTe₂, and Se₂Te monolayers belong to P3m1 space group with C_{3v} point symmetry, as shown in Fig. 1(a, b). The optimized lattice constants are 4.03, 4.11, and 3.88 Å for STe₂, SeTe₂, and Se₂Te monolayers, respectively, which are consistent with the ones in the literatures¹⁸⁻²¹. To check the stability of these systems, in Fig. 1(d, e, f), we calculate the phonon dispersion along with a high symmetric path (Γ -M-K- Γ , see Fig. 1(c)) in the Brillouin zone, and the frequency of phonon is free of imaginary frequency, showing that these systems are dynamic stability, which can also be confirmed in the previous reports^{20,21}. In addition, the AIMD simulations show that these systems are thermally stable as a consequence of the energy and temperature always vibrate in small amplitude around a fixed value, as shown in Fig.1(h, i, g). To further determine the energy stability of the system, we calculate the cohesive energy according to the formula in the references²², as listed in Table I, and the results are compared with those in

other references^{20,21}. The cohesive energy of all negative values indicates that the systems are energetically stable. Then, we first calculate the band structures of those Janus monolayers. The spin-orbit coupling (SOC) effect is considered in the calculation of the band structures because of the heavy element Te in the system. The results show that the STe₂, SeTe₂, and Se₂Te monolayers are all indirect band-gap semiconductors with a band-gap of 0.74(1.23), 0.53(0.98), and 0.67(1.06) eV at PBE+SOC (HSE06+SOC) methods, respectively, which agrees well with the reports^{20,21}.

Before using the TransOpt code¹⁵ to calculate the electronic transport properties, several important parameters that need to be prepared are the electron (hole) deformation potential E_l , Young's modulus G , and the Fermi level E_f . The detailed input parameters are shown in Table I. C_{2D} is the 2D elastic modulus, which is calculated using the formula $C_{2D} = \frac{1}{S_0} \frac{\partial^2 E}{\partial(\Delta l/l_0)^2}$. By comparison, our calculated results are closer to the references²⁰. E is the total energy of the material under a small uniaxial strain ranging from -2% to $+2\%$ with a step of 0.5% . l_0 is the lattice constant of the equilibrium structure, Δl is the change in lattice constant. E_l is the deformation potential in the transport direction of the valence band maximum (VBM) and conduction band minimum (CBM), and its expression is $E_l = \frac{\partial E_{edge}}{\partial(\Delta l/l_0)}$, E_{edge} is the energy of VBM or CBM under small uniaxial strain. Through Table I, it is easy to find that our calculation results are consistent with the previous calculation results, indicating the correctness of the calculation.

TABLE I. The summarized elastic modulus C_{2D} of the 2D material, the deformation potentials E_l^{VBM} and E_l^{CBM} near the VBM and CBM, as well as Young's modulus G and the Fermi level E_f .

Compounds	C_{2D} (N/m)	E_l^{VBM} (eV)	E_l^{CBM} (eV)	G (GPa)	E_f (eV/atom)
Janus STe ₂	41.75	-4.34	-6.27	116.57	-1.69
	40.50 ²⁰				-3.35 ²⁰
	50.91 ²¹	3.92 ²¹	6.06 ²¹		-2.38 ²¹
Janus SeTe ₂	38.35	-4.78	-6.42	104.57	-2.00
	46.49 ²¹	4.36 ²¹	6.18 ²¹		-2.24 ²¹
Janus Se ₂ Te	42.9	-7.77	-9.72	124.97	-2.19

Fig.2 depicts the carrier-concentration-dependent Seebeck coefficient S and conductivity σ of Janus binary compounds. For both n-type doping and p-type doping, S monotonically decreases with the increase of carrier concentration, while σ exponentially increases with the increase of carrier concentration. The power factor PF , $PF = S^2\sigma$, hinder as a result of the strong coupling effect between S and σ , thereby limiting the thermoelectric figure of merit ZT . Therefore, the decoupling between Seebeck coefficient and conductivity has become an effective strategy for improving thermoelectric efficiency.

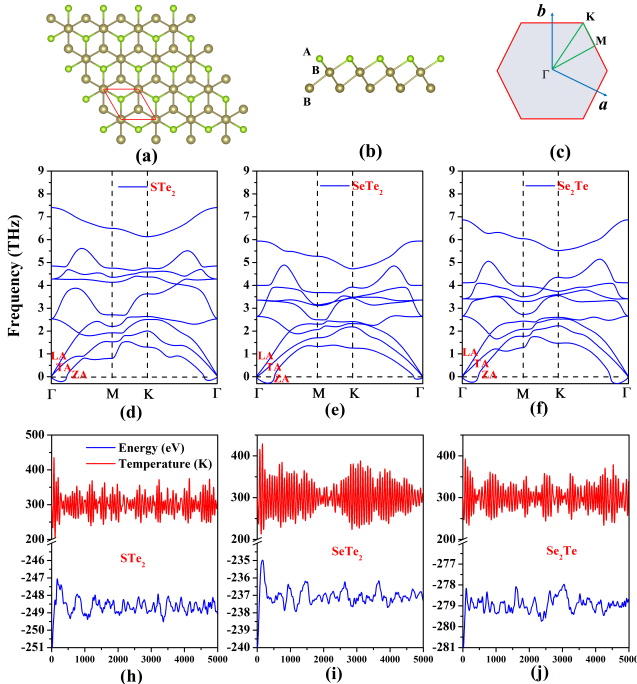


FIG. 1. (Color online) (a) and (b) represent the top and side view of Janus structures, respectively, together with the (c) first Brillouin zone high symmetric path. The phonon dispersions of (d) STe_2 , (e) SeTe_2 , (f) Se_2Te monolayers. The three low-frequency acoustic branches are divided into one out-of-plane vibration acoustic branch (ZA) and two in-plane transverse (TA) and longitudinal (LA) vibration acoustic branches. (h-j) represents the AIMD simulation: the variation of the total energy (blue) and temperature (red) with time.

It can be observed that in the vicinity of the optimal doping concentration range (the region where S and σ intersect), S tends to increase with increasing temperature. Conversely, σ decreases with increasing temperature. This is mainly because S is positively correlated with temperature T ²³:

$$S = \frac{8\pi^2 k_B^2}{3eh^2} m^* T \left(\frac{\pi}{3n} \right)^{2/3} \quad (1)$$

where m^* and n are the effective mass of electrons (holes) and the carrier concentration, respectively. The conductivity is positively related to mobility with the relationship:

$$\sigma = ne\mu = ne \frac{eh^3 C_{2D}}{k_B T m^* m_d E_l^2} \quad (2)$$

where the μ is carrier mobility, and n is carrier concentration. C_{2D} , E_l , k_B , m^* , and m_d are 2D in-plane elastic modulus, deformation potentials, Boltzmann constant, effective mass, and average effective mass, respectively. The scattering of carriers augments as a consequence of the increasing temperature, which induces a decrease in the mobility of carriers. Therefore, the con-

ductivity is inversely related to the temperature. At different temperatures (300 K, 400 K, 600 K), the power factor PF varies with the carrier concentration, as shown in Fig.3. Notably, the power factor PF gradually decreases with the increase of temperature. With a combination of temperature-dependent conductivity and the Seebeck coefficient discussed above, one can obtain that the decrease of PF with temperature is mainly caused by the decrease of conductivity with temperature. At 300 K, the maximum power factor of STe_2 and SeTe_2 is larger than that of Se_2Te . For example, the n-type (p-type) PF_{max} of STe_2 and SeTe_2 are 16.41 (43.81) $\times 10^{-4}$ W/mK² and 16.20 (35.73) $\times 10^{-4}$ W/mK² is larger than 13.81 (6.28) $\times 10^{-4}$ W/mK² of Se_2Te , which is may mainly because the first two materials contain two Te elements with optimal thermoelectric properties. The PF_{max} of these three materials is comparable to those of typical excellent thermoelectric materials such as SnSe (4 $\times 10^{-3}$ W/mK² at 300 K), Bi₂Te₃ ($\sim 3.5 \times 10^{-3}$ W/mK² at 300 K), PbTe ($\sim 2.5 \times 10^{-3}$ W/mK² at 500 K), 1T[']-phase MoSe₂ ($\sim 6 \times 10^{-3}$ W/mK² at 200-500 K), and doped MoS₂ (2.98×10^{-3} W/mK²)²⁴⁻²⁸, indicating that STe_2 , SeTe_2 , and Se_2Te are high-performance 2D thermoelectric materials.

However, it cannot be ignored that there is a big difference between the references data²¹ and our calculation results, which may be caused by the use of different calculation parameters and calculation software. BoltzTraP, which realizes the calculation of transport coefficient based on Boltzmann transport theory, is the most widely used program by far. However, BoltzTraP adopts the approximate method of constant relaxation time, which can only calculate the ratio of conductivity, electron thermal conductivity, and other coefficients to the relaxation time. Hence, to determine the electrical transport properties, the value of relaxation time must be set by the simulation experiment or calculations. The relaxation time is closely related to the effective mass of the electron and hole, $\tau = \frac{\mu m^*}{e}$ (τ , μ , m^* are the relaxation time, carrier mobility, and effective mass, respectively). It is well known that the calculation process of fitting the effective mass of the electron and hole with the energy band data is complicated and easy to causes errors. Thus, the dependence on the relaxation time constant introduces uncertainty in the calculation of electrical transport properties and limits the accuracy of its prediction. In contrast, the constant electro-acoustic coupling approximation method is used in the TransOpt software package, which can predict the relaxation time under phonon action and improve the accuracy of the prediction results of electrical transport properties such as conductivity. Thus, our calculations may be more accurate and reliable.

TABLE II. The calculated lattice thermal conductivity k_l is compared with the ones in other reports calculated by the different methods and n^{th} nearest neighbors, as well as the effective thicknesses d , and the n-(p)-type maximum power factor PF_{max} and the maximum ZT_{max} at room temperature.

Compounds		k_l (W/mK)	d (Å)	PF_{max} (10^{-4} W/mK ²)	ZT_{max}
Janus STe ₂	this work	0.2[9 th , ShengBTE, iteration]	7.12	16.41(43.81)[TransOpt]	2.11(2.09)
		~0.7[5 th , ShengBTE, iteration]			
	other work ²⁰	1.16[5 th , phono3py, iteration]	7.18		
other work ²¹		1.18[17 th , AlmaBTE, iteration]	7.20	83(350)[BoltzTraP2]	1.16(2.4)
		0.39[17 th , AlmaBTE, RTA]			
Janus SeTe ₂	this work	0.133[7 th , ShengBTE, iteration]	7.58	16.20(35.73)[TransOpt]	3.28(4.24)
		0.73[17 th , AlmaBTE, iteration]			
	other work ²¹	0.32[17 th , AlmaBTE, RTA]	7.79	85(340)[BoltzTraP2]	1.58(3.1)
Janus Se ₂ Te	this work	4.81×10^{-4} [9 th , ShengBTE, iteration]	7.39	13.81(6.28)[TransOpt]	3.40(6.51)

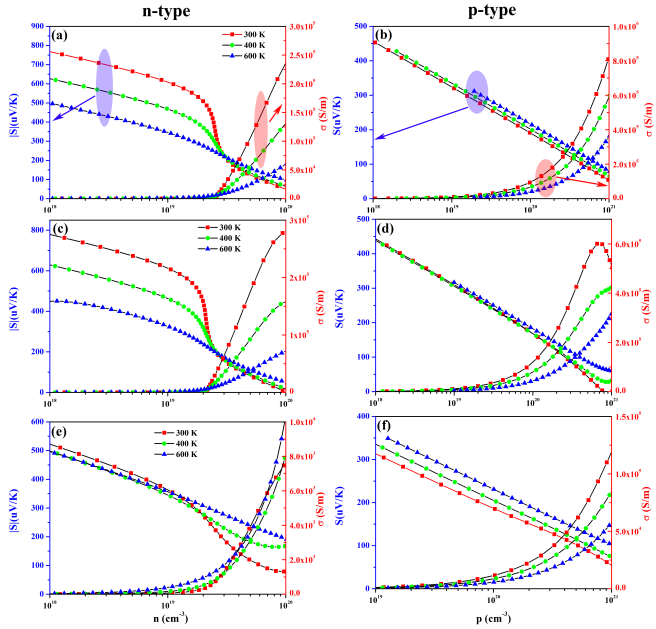


FIG. 2. (Color online) Seebeck coefficient S and conductivity σ of (a, b)STe₂, (c, d)SeTe₂ and (e, f)Se₂Te as a function of doping concentration at different temperatures. The light blue and light red areas in the figure help to distinguish between the S and σ corresponding to the ordinate.

B. Thermal transport properties

Currently, a very effective method to obtain lattice thermal conductivity is combining first-principles calculations based on an anharmonic lattice dynamics method with the phonon Boltzmann transport equation. This method involves the calculation of interatomic force constants (IFCs) with the harmonic IFCs and the higher-order IFCs^{29,30}. To obtain satisfactory lattice thermal conductivity k_l , the convergence of the cutoff radius for

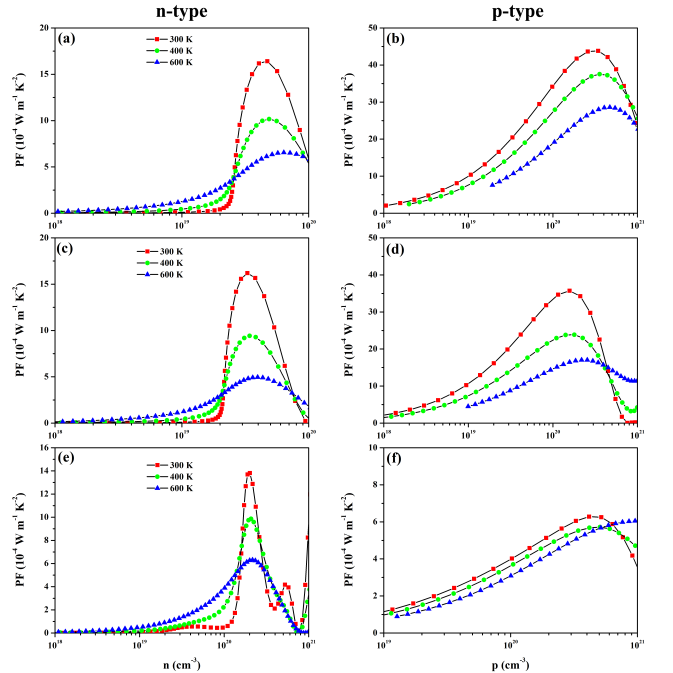


FIG. 3. (Color online) Power factor PF of (a, b) STe₂, (c, d) SeTe₂ and (e, f) Se₂Te as a function of doping concentration at different temperatures.

anharmonic interatomic force constants (IFCs) is tested. However, it is not easy to evaluate higher-order IFCs in comparison to harmonic IFCs. Hence, we use the root mean square (RMS)^{31,32} to evaluate the strength of interatomic interactions, which consist of the elements of the harmonic IFC tensor, that is

$$RMS(\Phi_{ij}) = \left[\frac{1}{9} \sum_{\alpha, \beta} \left(\Phi_{ij}^{\alpha\beta} \right)^2 \right]^{\frac{1}{2}} \quad (3)$$

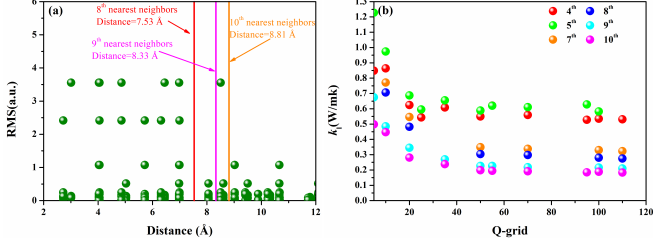


FIG. 4. (a) The relationship between the RMS of STe_2 and the cutoff radius reveals the distant interaction between atoms. (b) Convergence test of lattice thermal conductivity k_l of STe_2 with the change of Q grid when considering different cutoff radius.

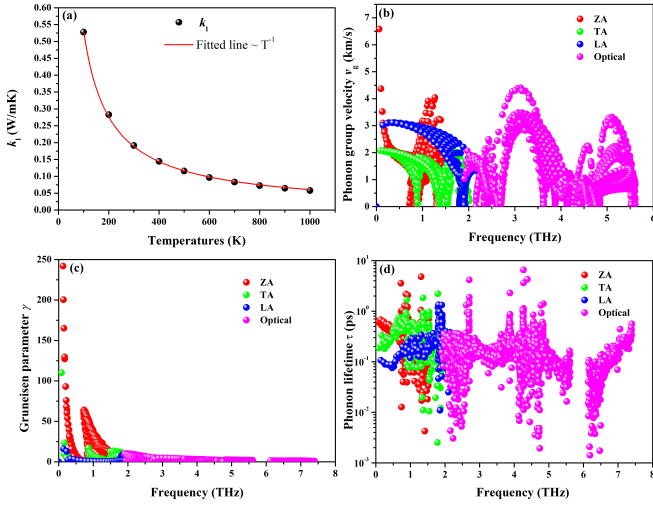


FIG. 5. (Color online) For STe_2 monolayer, (a) the lattice thermal conductivity k_l (black sphere) various with temperatures, and the fitted curve (solid red line) conform to the T^{-1} law. (b) shows the phonon group velocity v_g^2 as a function of phonon frequency. (c) represents the Grneisen parameter as a function of phonon frequency. (d) represents the phonon lifetime as a function of phonon frequency, with different colored spheres representing ZA (red sphere), TA (green sphere), LA (blue sphere), and Optical (magenta sphere) branches, respectively.

where the Φ_{ij} represents the second-order IFCs tensor. Large RMS can roughly reveal large interaction strengths^{31,32}. The longer the interatomic distance, the smaller the interatomic force and anharmonic interaction³³. Taking the STe_2 monolayer as an example, RMS can be calculated by calculating the second-order force tensor, as shown in FIG. 4(a). It can be seen that the value of the RMS tends to decrease with the increase of interatomic distance. Combined with the analysis in FIG. 4(b), it can be found that the cutoff distance of binary Janus STe_2 monolayer is as high as 8.33 Å (the 9th nearest neighbor) with strong anharmonic interaction, and the k_l with good convergence can be obtained, which is very close to that of the 10th nearest neighbor. Therefore, the lattice

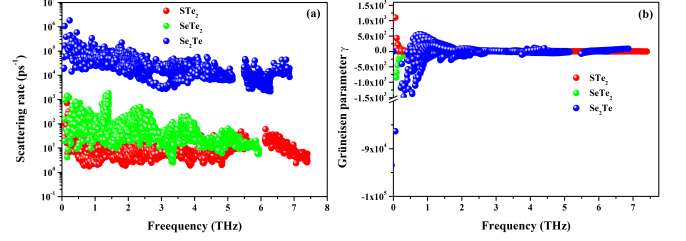


FIG. 6. (Color online) (a) Phonon scattering rate and (b) Grneisen parameters of Janus systems.

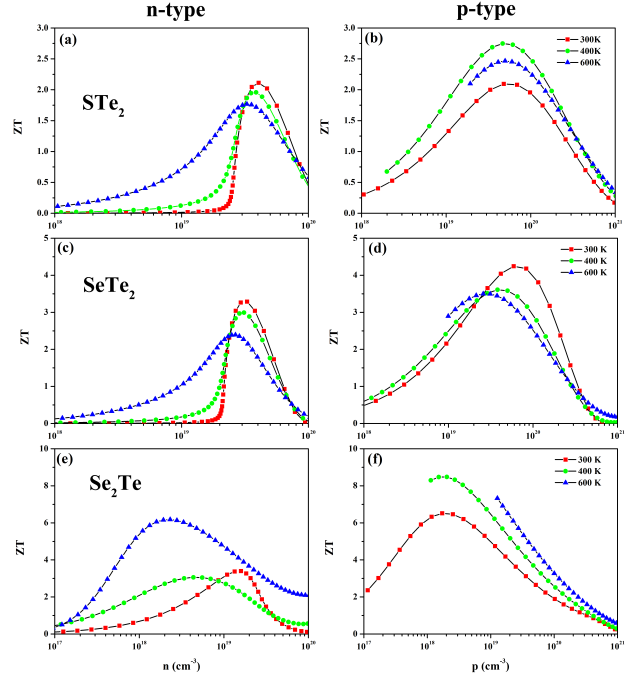


FIG. 7. (Color online) The figure of merit ZT of (a, b) STe_2 , (c, d) SeTe_2 , and (e, f) Se_2Te monolayers as a function of doping concentration and temperature.

thermal conductivity of STe_2 takes the calculation result of the 9th-order nearest neighbor, which balances the calculation accuracy and the calculation cost. Using the same method, after testing and analysis, the 7th and 8th nearest neighbors of SeTe_2 and Se_2Te can be used to obtain satisfactory converges of lattice thermal conductivity k_l .

As summarized in Table II, when taking the van der Waals radius of the element into account⁷, the corresponding effective thicknesses of Te_2S , Te_2Se , and Se_2Te are 7.12, 7.58, and 7.39 Å, respectively, in good agreement with other results^{20,21}. According to the normalization formula for 2D materials, we obtain the converges lattice thermal conductivities of 0.2, 0.133, and 4.81×10^{-4} W/mK for STe_2 , SeTe_2 , and Se_2Te 300 K, respectively (see Table II). These values are smaller than that of the same family monolayers α -Te (9.84 W/mK)³⁴,

α -Se (3.04 W/mK)³⁵, square-Te (0.61 W/mK), and square-Se (2.33 W/mK)³⁶, illustrating that Janus STe₂, SeTe₂, and Se₂Te monolayers have excellent thermoelectric properties. Combined with Fig. 4(b) and other calculation data, it can be found that the selection of cutoff radius (n^{th} -order nearest neighbor) plays a vital role in the accuracy and convergence of lattice thermal conductivity, that is, only by selecting a large enough cutoff radius can the lattice thermal conductivity with good convergence be obtained. Furthermore, the use of different computing software (ShengBTE or phono3py, or AlmaBTE) and computing methods (iteration or RTA) also has a large impact on the results. Ultra-low k_l value is attributed to the strong coupling effect between the acoustic mode and the low-frequency optical branch (FIG.1(d, e, f)), which results in strong photoacoustic interactions that suppress phonon transmission.

To further insight into the origin of the ultra-low lattice thermal conductivity, the phonon group velocity (v_g), the Grneisen parameter (γ), and the phonon lifetime (τ) of STe₂ monolayer are plotted in Fig.5. The average phonon group velocity of Janus α -STe₂ (0.77 km/s) is lower than that of α -TeSSe (0.84 km/s)³⁷, which is responsible for the lower lattice thermal conductivity of Janus α -STe₂, because k_l is proportional to the phonon group velocity squared (v_g^2). In addition, the larger γ parameter of α -STe₂ means larger anharmonicity resulting from the phonon scattering, which limits phonon transport and thus leads to lower k_l values. Furthermore, the relatively small phonon lifetime τ plays a dominant role in the lattice thermal conductivity. Especially, the phonon lifetime of the acoustic branches (ZA, TA, and LA). This also reasonably explains the small value of k_l . Furthermore, one can see that the Janus Se₂Te has the lowest lattice thermal conductivity in these three systems, which can deduce from that it possess the largest phonon scattering rate and the Grneisen parameter, as plotted in Fig. 6. In conclusion, the ultra-low lattice thermal conductivity origin from the i) strong coupling effect between the acoustic mode and the low-frequency optical branch, ii) low phonon group velocity, iii) small phonon lifetime, and iv) large anharmonicity.

Finally, combining the calculated thermoelectric power factor PF , lattice thermal conductivity k_l , and electron thermal conductivity k_e , we calculate the figure of merit (ZT) of the three materials at 300, 400 and 600 K temperatures, as shown in Fig.7. At the same temperature, the ZT of the three materials increases first and then decreases with the carrier concentration, regardless of the n-type or p-type carrier type. Considering the effect of temperature, only the n-type ZT of STe₂ and the n(p)-type ZT of SeTe₂ decrease with the increase of temperature, while there is no obvious rule for the other types. This is mainly due to the coupling effect among the Seebeck

coefficient, conductivity, electronic thermal conductivity, and lattice thermal conductivity, which check and balance each other and change with the temperature change. Therefore, there is no clear rule to follow between ZT and temperature. As listed in Table II, at 300 K, the maximum ZT values of n-type (p-type) carrier doping of STe₂, SeTe₂ and Se₂Te are 2.11 (2.09), 3.28 (4.24) and 3.40 (6.51), respectively, which are comparable to or even better than the classical thermoelectric materials SnSe (2.63, 2.46), SnS (1.75, 1.88), GeSe (1.99, 1.73)³⁸. By comparison, the calculated results agree with the ones in the reference.²¹. Those results show that STe₂, SeTe₂, and Se₂Te are thermoelectric materials with excellent performance and have great potential in thermoelectric device applications.

IV. CONCLUSION

We systematically studied the electrical transport, thermal transport, and thermoelectric properties of Janus STe₂, SeTe₂, and Se₂Te monolayers by first-principles calculations. We illustrate the opposite dependence of the Seebeck coefficient and conductivity on temperature. The decrease of PF with temperature is mainly caused by the decrease of σ . To obtain accurate and convergent lattice thermal conductivity, we calculate RMS to obtain a reasonable cutoff radius for the calculation of third-order forces. The selection of cutoff radius (n^{th} -order nearest neighbor) plays a vital role in the accuracy and convergence of lattice thermal conductivity. At room temperature, Janus STe₂, SeTe₂, and Se₂Te monolayers exhibit ultra-low lattice thermal conductivity of 0.2, 0.133, and 4.81×10^{-4} W/mK, which result from the strong coupling effect between the acoustic mode and the low-frequency optical branch, low phonon group velocity, small phonon lifetime, and large anharmonicity. Hence, high ZT values of 2.11 (2.09), 3.28 (4.24), and 3.40 (6.51) for n-type (p-type) carrier doping of STe₂, SeTe₂, and Se₂Te are obtained, indicating that they have important applications in the field of thermoelectric devices.

Conflicts of interest: There are no conflicts to declare.

ACKNOWLEDGMENTS

This work was supported by the National Natural Science Foundation of China (Grant No. 12074274), the National Natural Science Foundation of China Academy of Engineering Physics and jointly set up “NSAF” joint fund (Grant No. U1830101).

¹ H. Babaei, J. M. Khodadadi, and S. Sinha, *Appl. Phys. Lett.* **105**, 193901 (2014).

² C. Chang, M. Wu, D. He, Y. Pei, C. F. Wu, X. Wu, H. Yu,

- F. Zhu, K. Wang, and Y. Chen, *Science* **360**, 778 (2018).
- ³ L. D. Zhao, S. H. Lo, Y. Zhang, H. Sun, G. Tan, C. Uher, C. Wolverton, V. P. Dravid, and M. G. Kanatzidis, *Nature* **508**, 373 (2014).
- ⁴ J. Chen, Y. Dai, Y. Ma, X. Dai, W. Ho, and M. Xie, *Nanoscale* **9**, 15945 (2017).
- ⁵ Z. L. Zhu, X. L. Cai, S. H. Yi, J. L. Chen, Y. W. Dai, C. Y. Niu, Z. X. Guo, M. H. Xie, F. Liu, J. H. Cho, Y. Jia, and Z. Y. Zhang, *Phys. Rev. Lett.* **119**, 106101 (2017).
- ⁶ Z. Shi, R. Cao, K. Khan, A. K. Tareen, X. Liu, W. Liang, Y. Zhang, C. Ma, Z. Guo, X. Luo, and H. Zhang, *Nano-Micro Lett.* **12**, 99 (2020).
- ⁷ Z. Gao, F. Tao, and J. Ren, *Nanoscale* **10**, 12997 (2018).
- ⁸ C. Lin, W. D. Cheng, G. Chai, and H. Zhang, *Phys. Chem. Chem. Phys.* **20**, 24250 (2018).
- ⁹ L. Ramirez-Montes, W. Lopez-Prez, R. Gonzalez-Hernandez, and C. Pinilla, *Int. J. Quantum Chem.* **120**, 26267 (2020).
- ¹⁰ S. Chen, W. Tao, Y. Zhou, Z. Zeng, X. Chen, and H. Geng, *Nanotechnology* **32**, 455401 (2021).
- ¹¹ X. Zhong, Y. Huang, and X. Yang, *Mater. Res. Express* **8**, 045507 (2021).
- ¹² G. Kresse and J. Furthmüller, *Phys. Rev. B* **54**, 11169 (1996).
- ¹³ G. Kresse and D. Joubert, *Phys. Rev. B* **59**, 1758 (1999).
- ¹⁴ A. Togo, F. Oba, and I. Tanaka, *Phys. Rev. B* **78**, 134106 (2008).
- ¹⁵ X. Li, Z. Zhang, J. Xi, D. J. Singh, Y. Sheng, J. Yang, and W. Zhang, *Comp. Mater. Sci.* **186**, 110074 (2021).
- ¹⁶ Baroni, D. Gironcoli, Stefano, D. Corso, and Paolo, *Rev. Mod. Phys.* **73**, 515 (2001).
- ¹⁷ W. Li, J. Carrete, N. A. Katcho, and N. Mingo, *Comput. Phys. Commun.* **185**, 1747 (2014).
- ¹⁸ Y. Chen, J. Y. Liu, J. B. Yu, Y. G. Guo, and Q. Sun, *Phys. Chem. Chem. Phys.* **21**, 1207 (2019).
- ¹⁹ M. Sharma, *Mater. Sci. Eng. B* **280**, 115692 (2022).
- ²⁰ J. Singh, M. Jakhar, and A. Kumar, *Nanotechnology* **33**, 215405 (2022).
- ²¹ G. Liu, A. Guo, F. Cao, W. Ju, Z. Wang, H. Wang, G.-L. Li, and Z. Gao, *Phys. Chem. Chem. Phys.* (2022), [10.1039/D2CP03659B](https://doi.org/10.1039/D2CP03659B).
- ²² Y. Ding and Y. Wang, *Nanoscale Research Letters* **10**, 13 (2015).
- ²³ G. J. Snyder and E. S. Toberer, *Nat. Mater.* **7**, 105 (2008).
- ²⁴ J. P. Heremans, V. Jovovic, E. S. Toberer, A. Saramat, K. Kurosaki, A. Charoenphakdee, S. Yamanaka, and G. J. Snyder, *Science* **321**, 554 (2008).
- ²⁵ K. Hippalgaonkar, Y. Wang, Y. Ye, D. Y. Qiu, H. Zhu, Y. Wang, J. Moore, S. G. Louie, and X. Zhang, *Phys. Rev. B* **95**, 115407 (2017).
- ²⁶ H. K. Ng, A. Abutaha, D. Voiry, I. Verzhbitskiy, Y. Cai, G. Zhang, Y. Liu, J. Wu, M. Chhowalla, G. Eda, and K. Hippalgaonkar, *ACS Appl. Mater. Interfaces* **11**, 12184 (2019).
- ²⁷ J. Y. Oh, J. H. Lee, S. W. Han, S. S. Chae, E. J. Bae, Y. H. Kang, W. J. Choi, S. Y. Cho, J.-O. Lee, H. K. Baik, and T. I. Lee, *Energy Environ. Sci.* **9**, 1696 (2016).
- ²⁸ L. D. Zhao, G. Tan, S. Hao, J. He, Y. Pei, H. Chi, H. Wang, S. Gong, H. Xu, V. P. Dravid, C. Uher, G. J. Snyder, C. Wolverton, and M. G. Kanatzidis, *Science* **351**, 141 (2016).
- ²⁹ Y. Wang, A. K. Vallabhaneni, B. Qiu, and X. Ruan, *Nanoscale Microsc. Therm.* **18**, 155 (2014).
- ³⁰ A. Ward, D. A. Broido, D. A. Stewart, and G. Deinzer, *Phys. Rev. B* **80**, 125203 (2009).
- ³¹ O. Hellman, P. Steneteg, I. A. Abrikosov, and S. I. Simak, *Phys. Rev. B* **87**, 104111 (2013).
- ³² G. Qin and M. Hu, *Npj Comput. Mater.* **4**, 3 (2018).
- ³³ N. Wang, C. Shen, Z. Sun, H. Xiao, H. Zhang, Z. Yin, and L. Qiao, *ACS Appl. Energ. Mater.* **5**, 2564 (2022).
- ³⁴ Z. Gao, G. Liu, and J. Ren, *ACS Appl. Mater. Interfaces* **10**, 40702 (2018).
- ³⁵ G. Liu, Z. Gao, G. L. Li, and H. Wang, *J. Appl. Phys.* **127**, 065103 (2020).
- ³⁶ C. Lin, W. Cheng, G. Chai, and H. Zhang, *Phys. Chem. Chem. Phys.* **20**, 24250 (2018).
- ³⁷ S. B. Chen, X. R. Chen, Z. Y. Zeng, H. Y. Geng, and H. B. Yin, *Phys. Chem. Chem. Phys.* **23**, 26955 (2021).
- ³⁸ A. Shafique and Y. H. Shin, *Sci. Rep.* **7**, 506 (2017).